On-Load Field Prediction in SPM Machines by a Subdomain and Magnetic Circuit Hybrid Model

Lijian Wu, *Senior Member, IEEE*, Hao Yin, Dong Wang, and Youtong Fang, *Senior Member, IEEE*

***Abstract*—In this article, a new subdomain and magnetic circuit hybrid model (SMCHM) is proposed for on-load field prediction in the surface-mounted permanent-magnet machines. Equivalent current sheets are introduced to represent the nonlinearity effect, whose values are obtained by a magnetic circuit (MC) and correlated with boundary conditions in a subdomain model. The number of reluctances in the MC of the proposed model can be selected flexibly according to the nonlinearity effect. Instead of sectorial tooth in the conventional subdomain model, parallel tooth is considered in the proposed model to improve the accuracy. The SMCHM can accurately calculate the flux density distributions and electromagnetic performance considering the heavy nonlinearity effect under the load conditions with fast computation speed. The finite-element analysis is performed to validate the proposed model, which shows an excellent agreement between them. A prototype machine is manufactured to further prove these predictions.**

***Index Terms*—Hybrid model, magnetic circuit (MC), nonlinearity effect, permanent-magnet (PM) machine, subdomain model.**

I. Introduction

PERMANENT-MAGNET (PM) machines have higher torque/power density and efficiency compared to the conventional electrically excited machines because the rotor winding is substituted by rare-earth PM materials. Therefore, PM machines are widely used in electric vehicles, household appliances, wind power generators, industrial machines, and aerospace [1]–[4]. For machine design and optimization, it is important to choose an appropriate electromagnetic model. Generally, four modeling techniques are available, viz., numerical, analytical, magnetic circuit (MC), and hybrid models, to predict the flux density distributions and electromagnetic performance including back electromotive force (EMF), total torque, and some parasitic effects.

The applicable scopes of these four types of models are different according to their characteristics. Numerical methods, such as finite-element (FE) analysis, are very powerful [5]. FE method can accurately analyze the nonlinear motor with complex shapes, such as interior PM machines [3], [6], [7], [8], but it is time-consuming and cannot correlate electromagnetic performance with the motor size parameters. Although some commercial software packages have the function of parameter scanning for optimization, a faster tool is still preferred for initial design because of the wide range of candidates.

Therefore, an analytical method is often employed for initial motor design [9]–[11]. Some reviews for the one-dimensional (1-D), two-dimensional (2-D) slotless, and 2-D slotted analytical models can be found in [12] and [13]. As commonly used models accounting for slotting effect, the 2-D models includes a relative permeance model [14]–[17], a complex permeance model [18], [19], and a subdomain model [20]–[22]. The relative permeance and complex permeance models are both based on the conformal mapping, and the latter is more accurate but takes a much longer computational time. The subdomain model can accurately predict the magnetic field distribution for both radial and circumferential components. This model can directly solve the governing equations of every region and determine every coefficient by applying the boundary conditions. A review of the subdomain modeling techniques was provided in [23]. However, the three analytical models mentioned above have a basic assumption that the permeability of stator and rotor iron is infinite. Therefore, they bring relatively large error when the machines have heavy nonlinearity effect.

On the other hand, an MC method is another way to analyze the nonlinearity effect of electromagnetic performance besides the FE method [24]–[26]. The machine is equivalent to a magnetic network which consists of some nonlinear reluctances and magnetic sources according to the flux distribution. Based on Kirchhoff's law and the Newton–Raphson method, the nonlinear magnetic field distribution can be obtained. However, the MC method lacks accuracy because there are many assumptions

Manuscript received December 19, 2018; revised May 24, 2019 and August 1, 2019; accepted August 29, 2019. Date of publication September 25, 2019; date of current version April 30, 2020. This work was supported in part by the National Key R&D Program of China under Grant 2018YFB1501304 and in part by the National Natural Science Foundation of China under Grant 51677169 and Grant 51637009. *(Corresponding author: Lijian Wu.)*

L. Wu, H. Yin, and Y. Fang are with the College of Electrical Engineering, Zhejiang University, Hangzhou 310027, China (e-mail: ljw@zju.edu.cn; yinhzju@163.com; youtong@zju.edu.cn).

D. Wang is with the National Key Laboratory of Science and Technology on Vessel Integrated Power System, Naval University of Engineering, Wuhan 430000, China (e-mail: wangdongl@vip.sina.com).

Color versions of one or more of the figures in this article are available online at http://ieeexplore.ieee.org.

Digital Object Identifier 10.1109/TIE.2019.2942561

when the continuous iron or air gap is discretized to some reluctances.

Therefore, some hybrid models were proposed to combine the advantages of an analytical method and the MC method. There are some hybrid models based on conformal mapping [27]–[32]. However, these models cannot account for slot leakage accurately, because the magnetic field distribution in the slot is not predicted by the analytical models. The model proposed in [32] is only for the axial flux PM machines. Most importantly, the influence of iron saturation on the air-gap flux density distribution and torque is not considered in [32]. An MC and Fourier analysis hybrid model was developed for flux switching PM machine in [33]. This hybrid model essentially calculates the air-gap flux density by a subdomain model where the saturation effect is accounted for by artificially modifying the geometrical parameters, such as air-gap length or slot width. Such artificial modification is calibrated by a nonlinear MC model. Since only one parameter is modified to emulate the saturation effect, the accuracy may not be high for the details of air gap distribution. In addition, although the accuracy of a subdomain model is calibrated by the MC model, the reference, i.e., the MC prediction, may not be of high accuracy, since the disadvantage of the MC model is not improved. Some hybrid models in [34]–[36] combined a slotless analytical model with a very fine MC model, but magnetic field distributions in slots are all calculated based on the MC method, which makes it difficult to ensure the accuracy. Moreover, the large number of nodes in the MC model slows down the computation.

This article proposes a subdomain and MC hybrid model (SMCHM) for on-load condition in the surface-mounted PM (SPM) machine. Equivalent current sheets are introduced to represent the nonlinearity effect and transformed to the boundary conditions. The principle was shown in the previous article of this series for an open-circuit condition [37]. The magnetic field distributions in slots and air gap are calculated accurately by the subdomain model, and MC only exists in stator core. Hence, the advantages of both subdomain and MC models, i.e., fast computation, accuracy, and ability for nonlinear calculation, are fully combined. This combination of two models based on the transformation from nonlinearity effect to boundary conditions is the main novelty of the proposed model for on-load field prediction in an SPM machine. On the other hand, considering that both slot leakage and nonlinearity effect for on-load condition increase significantly compared to which under the open-circuit condition, the SMCHM is improved in this article. First, the number of equivalent reluctances in the MC model can be appropriately increased according to the nonlinearity effect. In addition, parallel stator tooth is considered in the MC model and the accuracy is further improved.

II. Hybrid Model

A. Construction of SMCHM

The main idea that the magnetic potential drop can be replaced with equivalent current sheets in slots is shown in Fig. 1. Rotor yoke is usually not saturated in the motor design process. Hence, equivalent current sheets are only arranged on the stator slot sides. The nonlinear stator core in Fig. 1(a) is equivalent to linear material with current sheets in Fig. 1(b). By applying the boundary and interface conditions, the electromagnetic field can be obtained by solving governing equations of three subdomains, viz., PM, air gap, and slots.

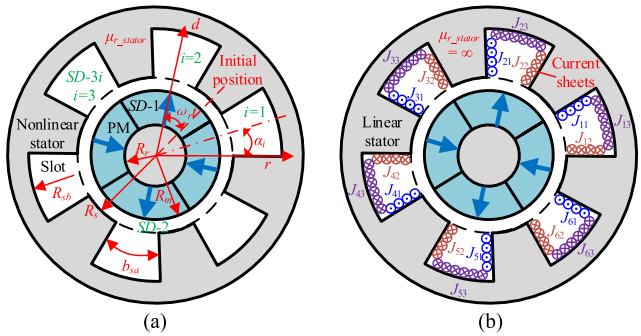

Fig. 1. Equivalent transformation of SMCHM. (a) Nonlinear model. (b) Linear model with equivalent current sheets.

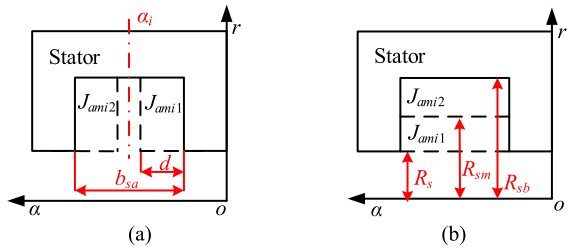

Fig. 2. Two types of winding layouts. (a) Nonoverlapping. (b) Overlapping.

In Fig. 1, ω_r is the angular velocity, α_i is the angle of the ith slot center line, r and α are the radial and circumferential positions, b_{sa} is the slot width angle, R_r, R_m, R_s, and R_{sb} are the radii of rotor yoke, magnet, slot top, and slot bottom, respectively, α_0 is the rotor initial position. J_{i1}, J_{i2}, and J_{i3} are the current densities of equivalent current sheets in the ith slot, and μ and μ_0 are the permeability of stator and vacuum.

Besides, two different types of winding layouts are shown in Fig. 2. J_{ami1} and J_{ami2} are the current densities of two armature coil sides in the ith slot. In Fig. 2(a), d is the width of one coil side. In Fig. 2(b), $R_{sm} = [(R_{sb}^2 + R_s^2)/2]^{1/2}$ to ensure the same area of two coil sides.

B. Improved Subdomain Model Under Load Condition

This section is to obtain the details of vector potential and flux density distributions of the solving field including *SD* 1, *SD* 2, and *SD* 3, viz., PMs, air gap, and slots. The vector potential distributions in the solving field satisfy Laplace's equation or Poisson's equation. Similar to the conventional subdomain model [20], solving these governing functions can obtain the general solutions with undetermined coefficients. Then, the interface conditions and boundary conditions are applied to calculate these undetermined coefficients. Subsequently, the flux densities in solving field are calculated based on the vector potential distributions. However, the boundary conditions in slots

are modified because of the equivalent current sheets. Therefore, these formulas have to be reworked as follows.

1) Vector Potential and Flux Density Distribution in Slots: The boundary conditions in the *i*th slot in *SD* 3 are

$$H_{3ri}\left|_{\alpha=\alpha_i+b_{sa}/2}\right. = J_{i1} \tag{1}$$

$$H_{3ri}\left|_{\alpha=\alpha_i-b_{sa}/2}\right. = -J_{i2} \tag{2}$$

$$H_{3\alpha i}\left|_{r=R_{sb}}\right. = -J_{i3}. \tag{3}$$

After solving Poisson's equation in slots [20], the general solution can be obtained.

For nonoverlapping winding machine, the general solution is

$$A_{z3i}(r,\alpha) = \sum_n A_{z3in}\cos\left[E_n\left(\alpha + b_{sa}/2 - \alpha_i\right)\right] + A_{z3i0} \tag{4}$$

where

$$A_{z3in} = \left(B_{3n}G_3 - \frac{E_nW_nR_{sb}}{\left(1-E_n^2\right)} - \frac{2\mu_0J_{amn}R_{sb}^2}{E_n\left(E_n^2-4\right)}\right)\left(\frac{r}{R_{sb}}\right)^{E_n} + B_{3n}\left(\frac{r}{R_s}\right)^{-E_n} + \frac{rE_n^2W_n}{1-E_n^2} + \frac{\mu_0J_{amn}r^2}{E_n{}^2-4} \tag{5}$$

$$A_{z3i0} = \mu_0J_{am0}\left(2R_{sb}^2\ln r - r^2\right)/4 + C_i\ln r - \mu_0\left(J_{i1}+J_{i2}\right)r/b_{sa} + Q_{3i} \tag{6}$$

where Q_{3i} and B_{3n} are undetermined constants and

$$W_n = 2\mu_0\left\{-\left(J_{i1}+J_{i2}\right)(-1)^n + J_{i2}\left[(-1)^n-1\right]\right\}/\left(E_n{}^2b_{sa}\right) \tag{7}$$

$$C_i = R_{sb}\left[\mu_0J_{i3} + \mu_0\left(J_{i1}+J_{i2}\right)/b_{sa}\right] \tag{8}$$

$$J_{iam0} = \left(J_{iam1}+J_{iam2}\right)/2 \tag{9}$$

$$J_{iamn} = 2\left(J_{iam1}-J_{iam2}\right)\sin\left(n\pi/2\right)/(n\pi) \tag{10}$$

$$E_n = n\pi/b_{sa} \tag{11}$$

$$G_3 = \left(R_s/R_{sb}\right)^{E_n}. \tag{12}$$

Then, the radial and circumferential flux densities can be calculated as

$$B_{3ir} = \sum_n B_{3irn}\sin\left[E_n\left(\alpha + b_{sa}/2 - \alpha_i\right)\right] \tag{13}$$

$$B_{3i\alpha}(r,\alpha) = \sum_n B_{3i\alpha n}\cos\left[E_n\left(\alpha + b_{sa}/2 - \alpha_i\right)\right] + B_{3i\alpha0} \tag{14}$$

where

$$B_{3irn} = -E_n\left\{\frac{E_n^2W_n}{\left(1-E_n{}^2\right)} + \frac{\mu_0J_{amn}r}{E_n^2-4} + \frac{B_{3n}}{R_s}\left(\frac{r}{R_s}\right)^{-E_n-1} + \left[\frac{B_{3n}G_3}{R_{sb}} - \frac{E_nW_n}{\left(1-E_n^2\right)} - \frac{2\mu_0J_{amn}R_{sb}}{E_n\left(E_n^2-4\right)}\right]\times\left(\frac{r}{R_{sb}}\right)^{E_n-1}\right\} \tag{15}$$

$$B_{3i\alpha n} = -\left[\left(\frac{B_{3n}E_nG_3}{R_{sb}} - \frac{E_n^2W_n}{1-E_n^2} - \frac{2\mu_0R_{sb}J_{amn}}{E_n^2-4}\right)\times\left(\frac{r}{R_{sb}}\right)^{E_n-1} - \frac{B_{3n}E_n}{R_s}\left(\frac{r}{R_s}\right)^{-E_n-1} + \frac{E_n{}^2W_n}{1-E_n^2} + \frac{2\mu_0J_{amn}r}{E_n^2-4}\right] \tag{16}$$

$$B_{3i\alpha0} = -\frac{\mu_0J_{am0}\left(R_{sb}^2/r - r\right)}{2} - \frac{C_i}{r} + \frac{\mu_0\left(J_{i1}+J_{i2}\right)}{b_{sa}}. \tag{17}$$

On the other hand, for an overlapping winding machine, the general solution for the bottom of the *i*th slot is

$$A_{zb3i}(r,\alpha) = \sum_n A_{zb3in}\cos\left[E_n\left(\alpha + b_{sa}/2 - \alpha_i\right)\right] + A_{zb3i0} \tag{18}$$

where

$$A_{zb3in} = \left(B_{3n}G_3 - E_nW_nR_{sb}/\left(1-E_n{}^2\right)\right)(r/R_{sb})^{E_n} + B_{3n}(r/R_s)^{-E_n} + rE_n^2W_n/\left(1-E_n^2\right) \tag{19}$$

$$A_{zb3i0} = -\mu_0\left(J_{i1}+J_{i2}\right)r/b_{sa} + C_i\ln r + \mu_0J_{iam2}\left(2R_{sb}{}^2\ln r - r^2\right)/4 + Q_{3bi}. \tag{20}$$

The general solution for the top of the *i*th slot is

$$A_{zt3i}(r,\alpha) = \sum_n A_{zt3in}\cos\left[E_n\left(\alpha + b_{sa}/2 - \alpha_i\right)\right] + A_{zt3i0} \tag{21}$$

where

$$A_{zt3in} = \left(B_{3tn}G_3 - E_nW_nR_{sb}/\left(1-E_n{}^2\right)\right)(r/R_{sb})^{E_n} + B_{3tn}(r/R_s)^{-E_n} + rE_n^2W_n/\left(1-E_n^2\right) \tag{22}$$

$$A_{zt3i0} = -\mu_0r\left(J_{i1}+J_{i2}\right)/b_{sa} + C_i\ln r + C_{ti}\ln r - \mu_0J_{iam1}r^2/4 + Q_{3ti}. \tag{23}$$

Interface conditions between the top and the bottom of the *i*th slot are applied, viz. that the vector potential and the circumferential flux densities are equal at $r = R_{sm}$, then

$$B_{3tn} = B_{3n} \tag{24}$$

$$C_{ti} = \mu_0J_{iam1}R_{sm}^2/2 + \mu_0J_{iam2}\left(R_{sb}^2 - R_{sm}^2\right)/2 \tag{25}$$

$$Q_{3bi} = Q_{3ti} + C_{ti}\ln R_{sm} - \mu_0J_{iam1}R_{sm}^2/4 - \mu_0J_{iam2}\left(2R_{sb}^2\ln R_{sm} - R_{sm}^2\right)/4. \tag{26}$$

Then, the radial and circumferential flux densities are

$$B_{b3ir} = \sum_n B_{b3irn} \sin\left[E_n\left(\alpha + b_{sa}/2 - \alpha_i\right)\right] \quad (27)$$

$$B_{b3ia} = \sum_n B_{b3ian} \cos\left[E_n\left(\alpha + b_{sa}/2 - \alpha_i\right)\right] + B_{b3ia0} \quad (28)$$

where

$$\begin{aligned} B_{b3irn} = & -(E_n/r)\left[\left(B_{3n}G_3\right.\right. \\ & - E_n W_n R_{sb}/\left(1-E_n^2\right)\left)(r/R_{sb})^{E_n}\right. \\ & \left.\left. + B_{3n}(r/R_s)^{-E_n} + rE_n^2 W_n/\left(1-{E_n}^2\right)\right)\right] \end{aligned} \quad (29)$$

$$\begin{aligned} B_{b3ian} = & -(E_n/r)\left[\left(B_{3n}G_3\right.\right. \\ & - E_n W_n R_{sb}/\left(1-{E_n}^2\right)\left)(r/R_{sb})^{E_n}\right. \\ & \left.\left. - B_{3n}(r/R_s)^{-E_n} + rE_n W_n/\left(1-E_n^2\right)\right)\right] \end{aligned} \quad (30)$$

$$\begin{aligned} B_{b3ia0} = & \mu_0\left(J_{i1}+J_{i2}\right)/b_{sa} - C_i/r \\ & - \mu_0 J_{iam2}\left(R_{sb}^2/r - r\right)/2 \end{aligned} \quad (31)$$

in the bottom of the *i*th slot and

$$B_{t3ir} = \sum_n B_{t3irn} \sin\left[E_n\left(\alpha + b_{sa}/2 - \alpha_i\right)\right] \quad (32)$$

$$B_{t3ia} = \sum_n B_{t3ian} \cos\left[E_n\left(\alpha + b_{sa}/2 - \alpha_i\right)\right] + B_{t3ia0} \quad (33)$$

where

$$B_{t3irn} = B_{b3irn} \text{ and } B_{t3ian} = B_{b3ian} \quad (34)$$

$$B_{t3ia0} = \mu_0\left(J_{i1}+J_{i2}\right)/b_{sa} - \left(C_i + C_{ti}\right)/r + \mu_0 J_{iam1} r/2 \quad (35)$$

in the top of the *i*th slot.

2) Vector Potential and Flux Density Distribution in PM and Air Gap: The solving process for magnetic field distribution in PM and air gap are same as [20]. It shows the expressions of vector potential A_{z1}, radial and circumferential flux densities B_{1r} and $B_{1\alpha}$ in the PM, together with the expressions of vector potential A_{z2}, radial and circumferential flux densities B_{2r} and $B_{2\alpha}$ in the air gap. These expressions contain some undetermined coefficients A_1, B_1, A_2, B_2, C_2, and D_2. These undetermined coefficients beside B_{3n} will be obtained by the interface conditions shown in Appendix A.

C. Nonlinearity Effect

Based on the improved subdomain model, it is very important to obtain the current density of every equivalent current sheet, viz., J_{i1}, J_{i2}, and J_{i3}. As Fig. 3 shows, a "π" type of MC, of which the number of nodes is flexible, is introduced to obtain these current density values. In this MC model, the number of equivalent reluctances in each stator tooth (N_{tooth}) and each stator yoke (N_{yoke}) can be selected, respectively. Essentially, the selection of number represents the discretization degree of magnetic field distribution. When there are great slot leakages and nonlinearity effect is heavy compared to an open-circuit condition, a relatively fine magnetic network will be needed.

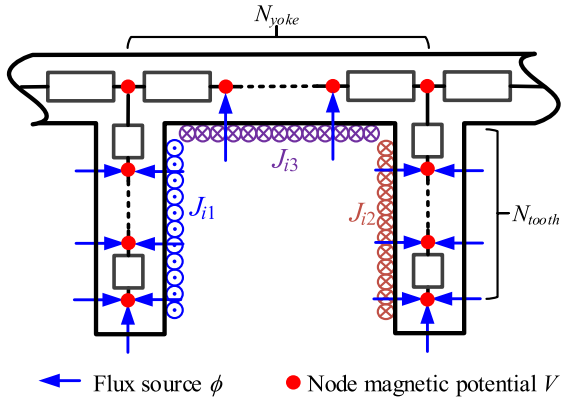

Fig. 3. Changeable MC of stator under load condition.

For the machines mentioned above in Table I, the MC shown as Fig. 4 is used, where $N_{yoke} = 2$, $N_{tooth} = 4$, and N_s is the number of stator teeth. The values of flux sources can be calculated from the radial or circumferential flux densities in slots and air gap by the subdomain model of the SMCHM.

Then, according to Kirchhoff's law, the node magnetic potential matrix is

$$\mathbf{V} = \left(\mathbf{A}\mathbf{\Lambda}\mathbf{A}^{\mathbf{T}}\right)^{-1}\mathbf{\Phi} \quad (36)$$

where $\mathbf{A}$ is the incidence matrix, $\mathbf{\Lambda}$ is the branch permeance matrix, and $\mathbf{\Phi}$ is the node flux matrix. The permeability of nonlinear iron is decided by flux passing through it. The values of every current sheet in the *i*th slot can be calculated from every node magnetic potential

$$J_{i1} = \left(V_{5Ns+i+1} - V_{2i+1}\right)/\left(R_{sb} - R_s\right) \quad (37)$$

$$J_{i2} = \left(V_{2i-1} - V_{5Ns+i}\right)/\left(R_{sb} - R_s\right) \quad (38)$$

$$J_{i3} = \left(V_{2i+1} - V_{2i-1}\right)/\left(R_{sb}\cdot b_{sa}\right) \quad (39)$$

where $R_{sb} - R_s$ and $R_{sb}\cdot b_{sa}$ are the current sheets lengths on the stator tooth edge and yoke edge in the slot, respectively.

D. Combination of MC and Subdomain of SMCHM

In the proposed SMCHM, the equivalent current densities used in the improved subdomain model are obtained by the MC, and the flux sources flowing to the MC are calculated by the improved subdomain model. Therefore, an iteration process is needed between the two models of the SMCHM to find the convergent solutions. After that, the electromagnetic performances including flux linkage, induced phase voltage, and total torque can be calculated and are shown in Appendix B.

III. FE and Experimental Validation

In order to validate the accuracy of the SMCHM, an FE analysis is used for two integer-slot and fractional-slot SPM machines whose main parameters are presented in Table I. The proposed MC of the SMCHM, as Fig. 3, is suitable for both kinds

TABLE I
MAIN PARAMETERS OF SPM MACHINES

Parameter	Machine A	Machine B	Unit
Stator outer radius	50	50	mm
Stator inner radius	27.85	29.5	mm
Air-gap length	0.5	0.5	mm
Magnet thickness	3.5	3	mm
Rotor outer radius	27.35	29	mm
Active length	50	50	mm
Tooth width	4.5	7	mm
Yoke height	3.2	3.5	mm
Pole-arc to pole-pitch ratio	1	1	
Magnet remanence	1.20	1.20	T
Relative recoil permeability	1.05	1.05	
Magnetization	Parallel	Parallel	
Rated speed	400	400	r/min
Number of pole pairs	4	4	
Number of slots	24	12	
Number of turns	30	45	
Rated current values (peak)	6.36	10	A
Lamination material	WG35WW300	WG35WW400	

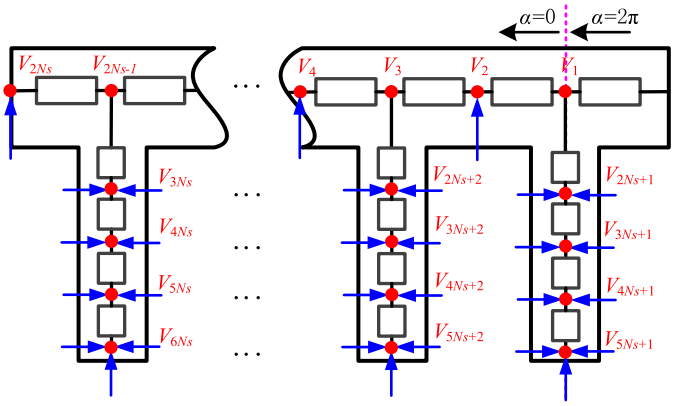

Fig. 4. MC of the stator under load condition.

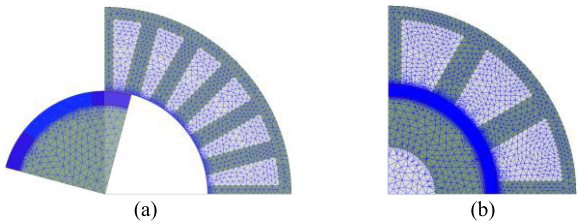

Fig. 5. Mesh plots in FE models. (a) Machine A. (b) Machine B.

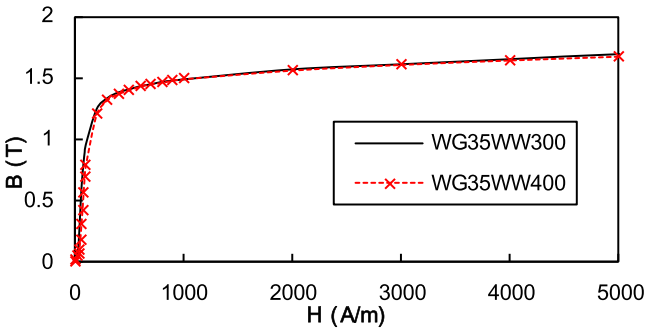

Fig. 6. *B–H* curve of stator material.

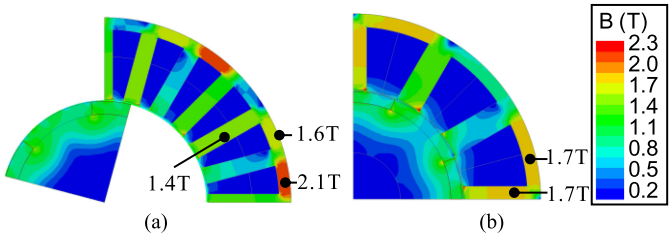

Fig. 7. Flux density predictions from FE analysis under load condition. (a) Machine A. (b) Machine B.

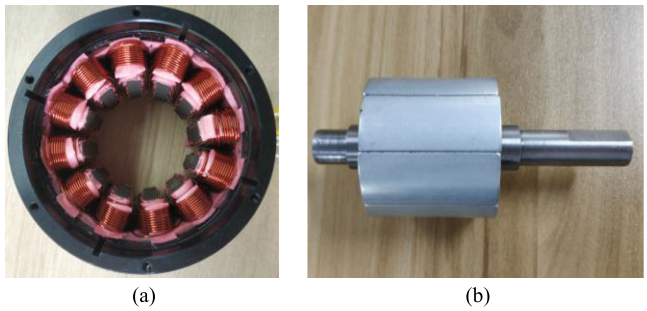

Fig. 8. Prototype machine of 8-pole/12-slot. (a) Stator. (b) Rotor.

of SPM machines, because the different fluxes flowing to the MC of the SMCHM caused by integer-slot and fractional-slot SPM are considered by the flux sources calculated by the improved subdomain model of the SMCHM. The MC of the SMCHM is only used for calculating the magnetic potential drops in stator in a specific magnetic field defined by the subdomain model of the SMCHM.

Fig. 5 shows the mesh plots used in the FE models. Fig. 6 shows the *B–H* curve of stator material. Fig. 7 shows the FE predicted flux densities of Machines A and B. Both of them are designed to have a high degree of saturation to highlight the difference between nonlinear and linear predictions. Compared with Machine A, Machine B has more saturated teeth but less saturated yoke. The maximum flux density in Machine A is 2.1 T, while it is 1.7 T in Machine B. Therefore, Machine A has heavier nonlinearity effect than Machine B. Fig. 8 shows the prototype machine of Machine B used for an experimental validation.

Figs. 9 and 10 are the flux density values of Machines A and B in the air gap predicted by the SMCHM, subdomain model, and FE models. The main harmonic components of radial flux densities in the two figures are given in Fig. 11. As they show, the results predicted by the SMCHM agree well with the nonlinear FE solutions, but the linear models always overestimate the radial flux density. The comparison of Machines A and B shows that the superiority on accuracy of the SMCHM is more obvious when the saturation effect is heavy.

Figs. 12–14 show the electromagnetic performances of Machines A and B, respectively, including flux linkage, induced

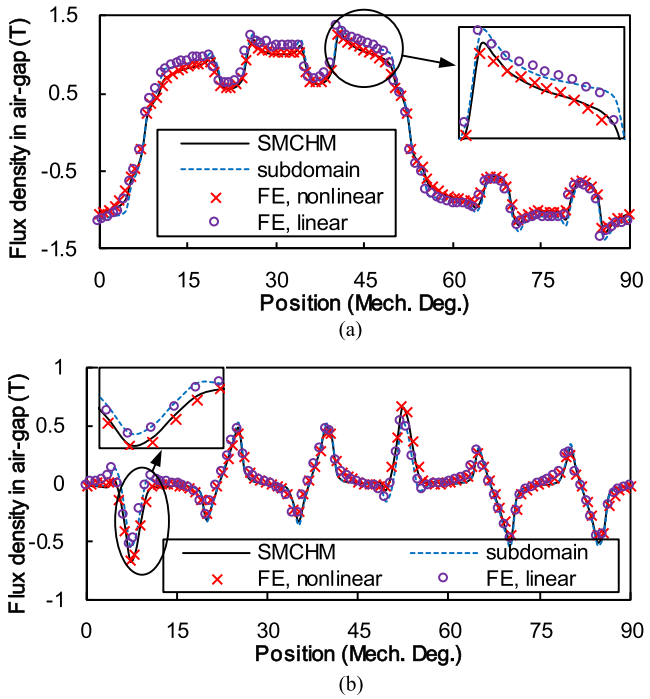

Fig. 9. Flux densities predicted by SMCHM, subdomain, and FE models in the middle of air gap of machine A under load condition. (a) Radial. (b) Circumferential.

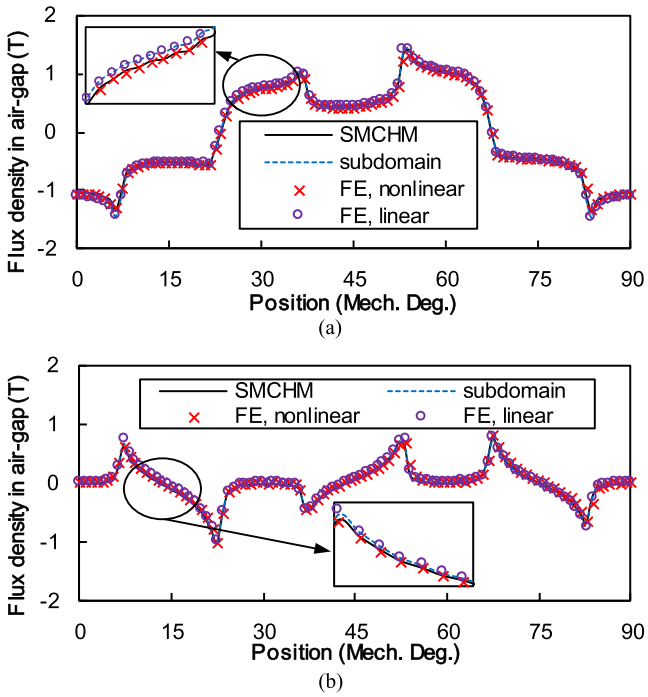

Fig. 10. Flux densities predicted by SMCHM, subdomain, and FE models in the middle of air gap of machine B under load condition. (a) Radial. (b) Circumferential.

voltage, and total torque. The results from the SMCHM and nonlinear FE model still show an excellent agreement, but the conventional subdomain model and the linear FE model still overestimates. The difference between the nonlinear and linear models is more significant in Machine A, because it is more saturated as mentioned earlier. Therefore, the SMCHM is a reliable model for motor design and parameter optimization because of the nonlinearity effect is considered.

Fig. 14 also contains the measurement of a prototype machine for total torque. Beside, Fig. 15 shows the back electromotive force (EMF) of the four models mentioned above and the measurement results of Machine B. There are some errors between the prediction of nonlinear FE model and the measurement of prototype machine around the crest due to manufacturing errors and the neglected end effect in the 2-D FE model. Overall, the SMCHM and nonlinear FE predictions agree very well with the measurement.

Fig. 16 shows the total torque varied with I_q predicted by the SMCHM, subdomain, and FE models, together with the measurement of prototype Machine B when $I_d = 0$A and the electrical degree of rotor position is 108°. At this position, the error caused by manufacturing and neglect of end effect in the 2-D FE model is the minimum, whilst the difference between the nonlinear and linear models is obvious, as shown in Fig. 14. Therefore, the nonlinearity effect can be highlighted, which is the focus of this article. At this position, the error between the prediction of nonlinear FE model and the measurement is relatively small, it can be observed that the predictions of linear FE model and the subdomain model are two straight lines, which shows they cannot consider nonlinearity effect. The measurements and predictions of the nonlinear FE model and the proposed SMCHM are three curves with excellent agreement, which proves high accuracy of the SMCHM for the saturated machines.

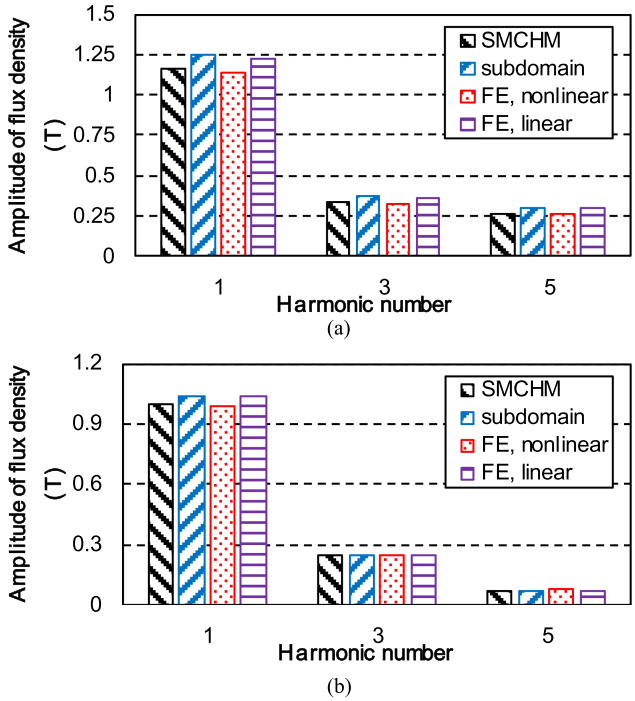

Fig. 11. Harmonic components of radial flux densities in air gap predicted by SMCHM, subdomain, and FE models under load condition. (a) Machine A. (b) Machine B.

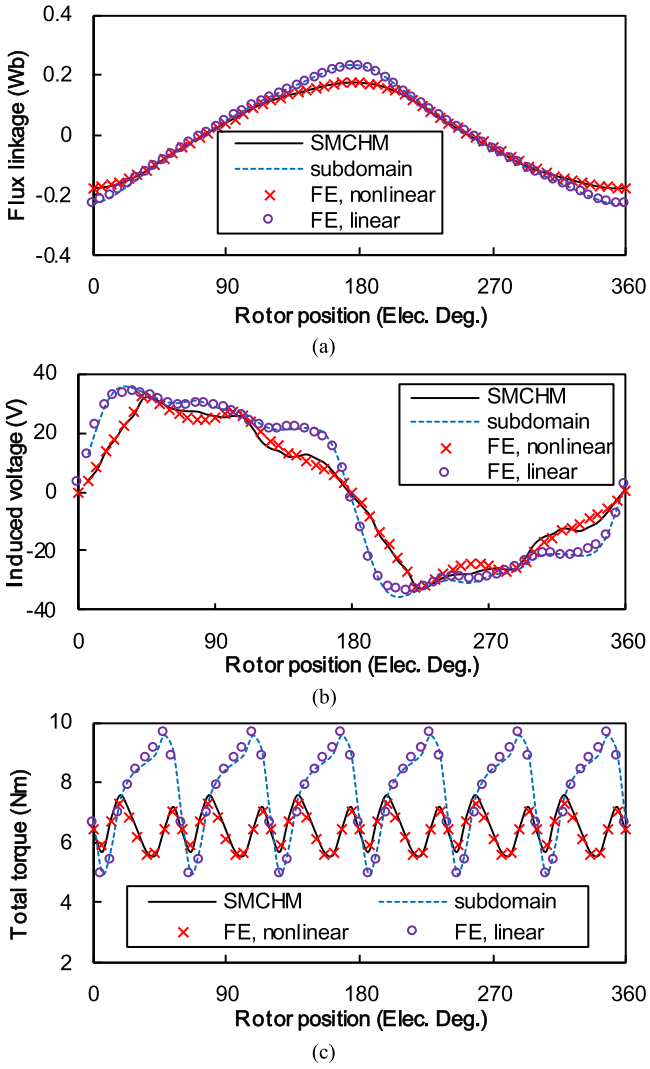

Fig. 12. Electromagnetic performances predicted by SMCHM, subdomain, and FE models of machine A under load condition. (a) Flux linkage. (b) Induced voltage. (c) Total torque.

TABLE II
CALCULATION TIME OF SMCHM, SUBDOMAIN, AND FE MODELS FOR TWO MACHINES (UNIT: s)

	SMCHM	Subdomain	FE nonlinear	FE linear
Machine A	16.92	0.78	287	216
Machine B	4.87	0.75	250	223

Beside, the calculation time of the SMCHM, subdomain, and FE models for Machine A/B in one electrical period including 61 field calculation points by a same computer whose CPU is i7-7700 is presented in Table II. The conventional subdomain and the developed hybrid models are calculated by Matlab scripts, while the FE models are performed on the Ansys Maxwell platform. The total elements in the FE models for Machine A/B are 23750/24336. It can be observed that the calculation time of the SMCHM increases with severer nonlinearity effect of an

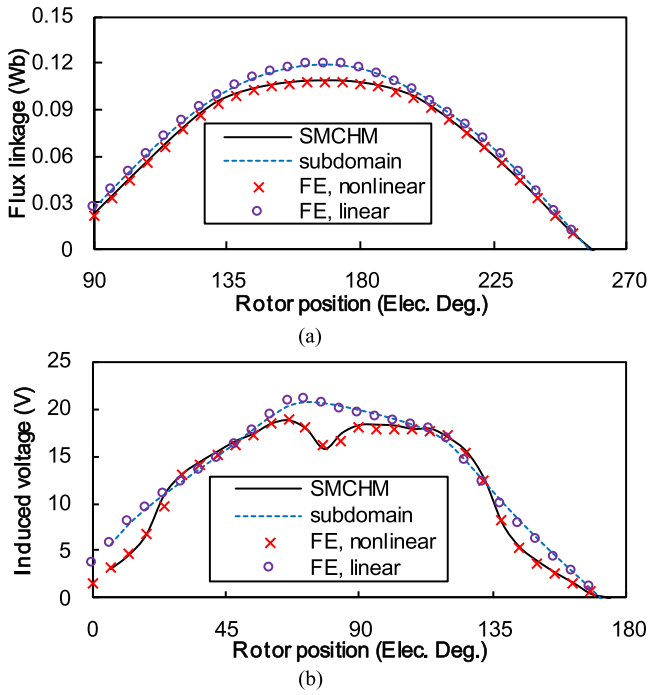

Fig. 13. Electromagnetic performances predicted by SMCHM, subdomain, and FE models of Machine B under load condition. (a) Flux linkage. (b) Induced voltage.

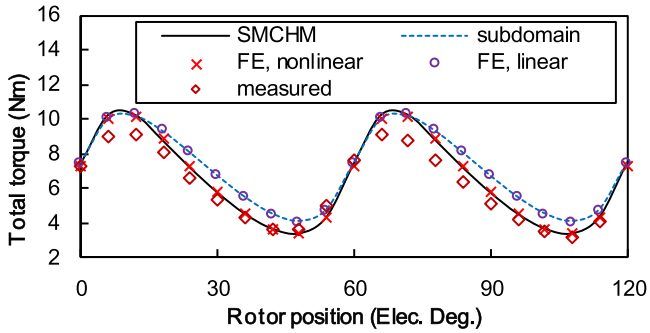

Fig. 14. Total torque predicted by SMCHM, subdomain, FE models, together with measurement of prototype Machine B under load condition.

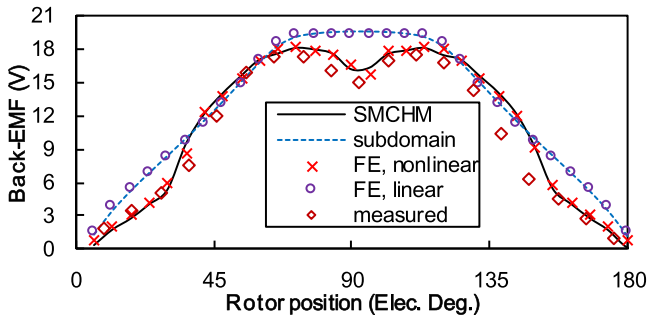

Fig. 15. Back EMF predicted by SMCHM, subdomain, FE models, together with measurement of prototype Machine B.

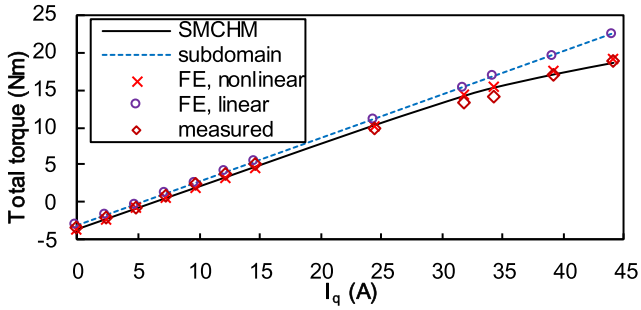

Fig. 16. Total torque varied with I_q predicted by SMCHM, subdomain, FE models, together with measurement of prototype Machine B, when $I_d = 0$ A and electrical degree of rotor position is 108°.

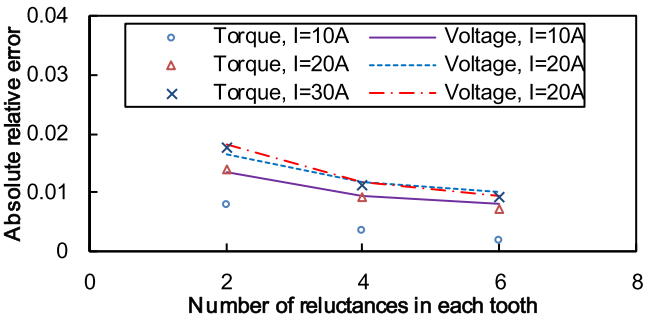

Fig. 17. Absolute relative errors of SMCHM predicted average torque and fundamental induced voltage compared to FE results of Machine B.

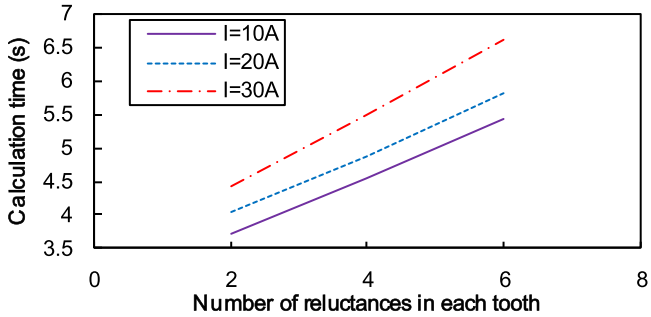

Fig. 18. Calculation time of SMCHM predicted average torque and fundamental induced voltage of Machine B.

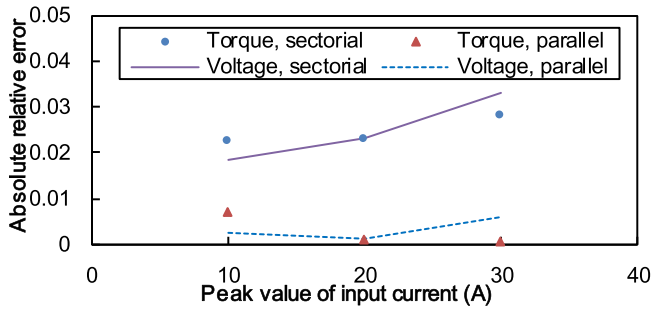

Fig. 19. Absolute relative errors of SMCHM predicted average torque and fundamental induced voltage compared to FE results of Machine B.

SPM machine, while it can still save 93% calculation time even when Machine A is extremely saturated.

The superiority of calculation speed and the excellent accuracy make the proposed SMCHM very suitable for machine optimization. Such optimization usually requires scanning many design parameters to search the best result, which is time-consuming by using the FE method. That is why some commercial tools with less accuracy but fast speed are still available on the market for machine design engineers. The proposed SMCHM can significantly improve their accuracy and keep similar speed, which can dramatically shorten development cycle.

In addition, the influence of the number of equivalent MC reluctances and consideration of parallel teeth in the proposed model is investigated. Machine B is still used in the investigation except the current value is variable to obtain different nonlinearity effect.

Fig. 17 shows the absolute relative errors of average torque and fundamental amplitude of induced voltage predicted by the SMCHM with different input currents and number of reluctances, compared to the FE predictions. Sectorial tooth is used in this FE model to exclude approximation brought by other factors. Overall, the relative errors decrease with the increase of reluctances number in each tooth, when the number of reluctances in each yoke is fixed to 2. Fig. 18 shows the calculation time of the SMCHM predicted for the results of Fig. 17. It can be observed that the calculation time increases as the number of reluctances in each yoke increases. Therefore, the selection of number of MC nodes is a tradeoff between the accuracy and computation time.

Moreover, the conventional subdomain model is based on the polar coordinate system, therefore, the tooth is approximated to have a sectorial shape [20]. However, the parallel tooth is more common in the practice. Therefore, in the hybrid model of this article, the parallel tooth is considered in the MC method to improve the accuracy, although the sectorial tooth is still used in the analytical equations. The predictions from the SMCHMs using sectorial tooth or parallel tooth are compared in Fig. 19. It shows absolute relative errors of average torque and fundamental amplitude of induced voltage of Machine B with reference to the FE analysis. The parallel tooth is used in the FE model. It is observed that the use of parallel tooth in the SMCHM can improve accuracy.

IV. Conclusion

In this article, we developed an SMCHM for the SPM machines under a load condition. Nonlinearity effect was considered by employing current densities of equivalent current sheets, which represented magnetic potential drop, as boundary conditions in the conventional subdomain model. Therefore, this hybrid model combined the advantages of the subdomain and MC models, such as fast computation speed, excellent accuracy, and considering nonlinearity effect. In addition, according to the nonlinearity effect, the number of MC reluctances could be selected flexibly for the tradeoff between the accuracy and computation time. Moreover, when machines with parallel tooth were analyzed, the real parallel shape could be accurately considered in the MC of the SMCHM to improve the accuracy.

The FE analysis had performed and the high consistency between the predictions of SMCHM and FE model validated the effectiveness of the SMCHM. The experimental results of prototype machine verified these predictions.

APPENDIX A

The equations to obtain those undetermined coefficients mentioned above are

$$B_{I\alpha} = B_{II\alpha} \text{ and } A_I = \mathrm{A}_{II}. \tag{40}$$

For a nonoverlapping winding machine, the circumferential flux density along the stator bore calculated by *SD* 3 is

$$B_{s\alpha} = \sum_k \left[C_s \cos(k\alpha) + D_s \sin(k\alpha)\right] \tag{41}$$

where

$$\begin{aligned} C_s &= \frac{1}{\pi}\sum_i \int_0^{2\pi} \left(B_{3i\alpha}|_{\mathrm{r}=R_s}\right)\cos(k\alpha)d\alpha \\ &= \sum_i B_{i\alpha 0}\eta_{i\alpha 0} + \sum_i\sum_n B_{i\alpha n}\eta_{i\alpha n} \end{aligned} \tag{42}$$

$$\begin{aligned} D_s &= \frac{1}{\pi}\sum_i \int_0^{2\pi} \left(B_{3i\alpha}|_{\mathrm{r}=R_s}\right)\sin(k\alpha)d\alpha \\ &= \sum_i B_{i\alpha 0}\varepsilon_{i\alpha 0} + \sum_i\sum_n B_{i\alpha n}\varepsilon_{i\alpha n} \end{aligned} \tag{43}$$

where

$$\begin{aligned} B_{i\alpha n} = -\Bigg[&\frac{E_n B_{3n}}{R_s}\left(G_3^2 - 1\right) + \frac{E_n^2 W_n}{1 - {E_n}^2}\left(1 - G_3\frac{R_{sb}}{R_s}\right) \\ &+ 2\mu_0 J_{amn}\left(R_s^2 - R_{sb}^2 G_3\right)/R_s\left(E_n^2 - 4\right)\Bigg] \end{aligned} \tag{44}$$

$$\begin{aligned} B_{i\alpha 0} = &-\mu_0 J_{am0}\cdot\frac{\left({R_{sb}}^2/R_s - R_s\right)}{2} \\ &+ \frac{\mu_0\left(J_{i1} + J_{i2}\right)}{b_{sa}} - \frac{C_i}{R_s} \end{aligned} \tag{45}$$

$$\eta_{i\alpha 0}(k) = 2\sin\left(kb_{sa}/2\right)\cos\left(k\alpha_i\right)/(k\pi) \tag{46}$$

$$\varepsilon_{i\alpha 0}(k) = 2\sin\left(kb_{sa}/2\right)\sin\left(k\alpha_i\right)/(k\pi) \tag{47}$$

$$\begin{aligned} \eta_{i\alpha n}(n,k) = &\, k/\left[\pi\left(k^2 - {E_n}^2\right)\right] \\ &\cdot\left[(-1)^n\sin\left(k\alpha_i + kb_{sa}/2\right)\right. \\ &\left.-\sin\left(k\alpha_i - kb_{sa}/2\right)\right] \end{aligned} \tag{48}$$

$$\begin{aligned} \varepsilon_{i\alpha n}(n,k) = &\, k/\left[\pi\left({E_n}^2 - k^2\right)\right] \\ &\cdot\left[(-1)^n\cos\left(k\alpha_i + kb_{sa}/2\right)\right. \\ &\left.-\cos\left(k\alpha_i - kb_{sa}/2\right)\right]. \end{aligned} \tag{49}$$

On the other hand, the circumferential flux density along the stator bore calculated by *SD* 2 is

$$\begin{aligned} B_{s\alpha} &= B_{2\alpha}|_{r=R_s} \\ &= -\left(1/R_s\right)\sum_k k\left(A_2 - B_2 G_2\right)\cos\left(k\alpha\right) \\ &\quad -\left(1/R_s\right)\sum_k k\left(C_2 - D_2 G_2\right)\sin\left(k\alpha\right) \end{aligned} \tag{50}$$

where

$$G_2 = \left(R_m/R_s\right)^k. \tag{51}$$

From (41) and (50), it can be obtained that

$$\begin{cases} -kA_2 + kB_2G_2 = R_sC_s \\ -kC_2 + kD_2G_2 = R_sD_s \end{cases}. \tag{52}$$

The vector potential along the stator bore in slots calculated by *SD* 2 is

$$A_s = \sum_n A_{2oi}\cos\left[E_n\left(\alpha + b_{sa}/2 - \alpha_i\right)\right] + A_{2oi0} \tag{53}$$

where

$$\begin{aligned} A_{2oi} &= \left(2/b_{sa}\right)\cdot\int_{\alpha_i - b_{sa}/2}^{\alpha_i + b_{sa}/2}\sum_k\left[A_{2c}\cos(k\alpha) + A_{2s}\sin(k\alpha)\right] \\ &\qquad\cdot\cos\left[E_n\left(\alpha + b_{sa}/2 - \alpha_i\right)\right]d\alpha \\ &= \sum_k\left(A_{2c}\sigma_i + A_{2s}\tau_i\right) \end{aligned} \tag{54}$$

$$A_{2oi0} = \sum_k\left(A_{2c}\sigma_{i0} + A_{2s}\tau_{i0}\right) \tag{55}$$

where

$$A_{2c} = A_2 + B_2G_2 \tag{56}$$

$$A_{2s} = C_2 + D_2G_2 \tag{57}$$

$$\sigma_i(n,k) = \left(2\pi/b_{sa}\right)\cdot\eta_i(n,k) \tag{58}$$

$$\tau_i(n,k) = \left(2\pi/b_{sa}\right)\cdot\varepsilon_i(n,k) \tag{59}$$

$$\begin{aligned} \sigma_{i0}(k) &= \left(b_{sa}/\pi\right)\cdot\eta_{i0}(k) \text{ and } \tau_{i0}(k) \\ &= \left(b_{sa}/\pi\right)\cdot\varepsilon_{i0}(k). \end{aligned} \tag{60}$$

The vector potential along the stator bore in slots calculated by *SD* 3 is

$$\begin{aligned} A_s &= A_{z3i}(r,\alpha)|_{r=R_s} \\ &= \sum_n A_{3oin}\cos\left[E_n\left(\alpha + b_{sa}/2 - \alpha_i\right)\right] + A_{3oi0} \end{aligned} \tag{61}$$

$$\begin{aligned} A_{3oin} = &\, B_{3n}\left(G_3^2 + 1\right) \\ &+ E_nW_n\left(R_sE_n - R_{sb}G_3\right)/\left(1 - E_n^2\right) \\ &+ \mu_0 J_{amn}\left[R_s^2 - 2R_{sb}^2G_3/E_n\right]/\left(E_n^2 - 4\right) \end{aligned} \tag{62}$$

$$\begin{aligned} A_{3oi0} = &\, \mu_0 J_{am0}\left(2{R_{sb}}^2\ln R_s - {R_s}^2\right)/4 + C_i\ln R_s \\ &- \mu_0\left(J_{i1} + J_{i2}\right)R_s/b_{sa} + Q_{3i}. \end{aligned} \tag{63}$$

From (53) and (61), it can be obtained that

$$A_{3oi} = A_{2oi} \text{ and } A_{3oi0} = A_{2oi0} \tag{64}$$

$$\begin{aligned} Q_{3i} = & \sum_k \left(A_{2c}\sigma_{i0} + A_{2s}\tau_{i0}\right) + \mu_0 \left(J_{i1} + J_{i2}\right) R_s/b_{sa} \\ & - R_{sb}\left[\mu_0 J_{i3} + \mu_0 \left(J_{i1} + J_{i2}\right)/b_{sa}\right] \ln R_s \\ & - \mu_0 J_{am0}\left(2R_{sb}^2 \ln R_s - R_s^2\right)/4. \end{aligned} \tag{65}$$

For an overlapping winding machine, the calculation process is the same as nonoverlapping except (44) and (45) are replaced by

$$B_{i\alpha n} = \frac{E_n B_{3n}}{R_s}\left(1 - G_3^2\right) + \frac{E_n^2 W_{\mathrm{n}}}{1 - E_n^2}\left(G_3 \frac{R_{sb}}{R_s} - 1\right) \tag{66}$$

$$\begin{aligned} B_{i\alpha 0} = & \mu_0 \left(J_{i1} + J_{i2}\right)/b_{sa} - \left(C_i + C_{ti}\right)/R_s \\ & + \mu_0 J_{iam1} R_s/2. \end{aligned} \tag{67}$$

Beside, (62), (63), and (65) are also replaced by

$$\begin{aligned} A_{3oin} = & B_{3n}\left(G_3^2 + 1\right) \\ & + E_n W_n \left(R_s E_n - R_{sb} G_3\right)/\left(1 - E_n^2\right) \end{aligned} \tag{68}$$

$$A_{3oi0} = C \ln R_s + C_t \ln R_s - \mu_0 \left(J_{i1} + J_{i2}\right) R_s/b_{sa} + Q_{3i} \tag{69}$$

$$\begin{aligned} Q_{3ti} = & \sum_k \left(A_{2c}\sigma_{i0} + A_{2s}\tau_{i0}\right) \\ & - \left(C_i + C_{ti}\right) \ln R_s + \mu_0 \left(J_{i1} + J_{i2}\right) R_s/b_{sa}. \end{aligned} \tag{70}$$

The interface conditions between air gap and PM are the same as [20]. Therefore, combining these interface conditions, the undetermined coefficients can be obtained.

Appendix B

Electromagnetic performance for both nonoverlapping and overlapping winding machine can also be calculated by vector potential distribution. For a nonoverlapping winding machine, the flux linkages with two coil sides in the *i*th slot are

$$\psi_{i1} = l_a \left(N_c/A_c\right)\left[Z_0 d + \sum_n \left(Z_n/E_n\right) \sin\left(E_n d\right)\right] \tag{71}$$

$$\psi_{i2} = l_a \left(N_c/A_c\right)\left[Z_0 d - \sum_n \left(Z_n/E_n\right) \sin\left(n\pi - E_n d\right)\right] \tag{72}$$

where

$$\begin{aligned} Z_0 = & \left(R_{sb}^2 - R_s^3\right) \cdot Q_{3i}/2 \\ & - \mu_0 \left(J_{i1} + J_{i2}\right)\left(R_{sb}^3 - R_s^3\right)/\left(3b_{sa}\right) \\ & - \mu_0 J_{am\,0}\left(R_{sb}^4 - R_s^4\right)/16 + \left(C_i + \mu_0 J_{am\,0} R_{sb}^2/2\right) \\ & \cdot \left[2R_{sb}^2 \ln R_{sb} - 2R_s^2 \ln R_s + R_s^2 - R_{sb}^2\right]/4 \end{aligned} \tag{73}$$

$$\begin{aligned} Z_n = & \left(B_{3in} G_3 - E_n W_{in} R_{sb}/\left(1 - E_n^2\right)\right) \\ & \times \left(R_{sb}^2 - G_3 R_s^2\right)/\left(E_n + 2\right) \\ & + B_{3in}\left(R_{sb}^2 G_3 - {R_s}^2\right)/\left(2 - E_n\right) \\ & + {E_n}^2 W_{in}\left(R_{sb}^3 - {R_s}^3\right)/\left[3\left(1 - E_n^2\right)\right] \\ & + \mu_0 J_{amn}\left(R_{sb}^4 - {R_s}^4\right)/\left[4\left({E_n}^2 - 4\right)\right] \\ & - 2\mu_0 J_{amn} R_{sb}^2 \left(R_{sb}^2 - G_3 R_s^2\right)/ \\ & \left[E_n\left(E_n^2 - 4\right)\left(E_n + 2\right)\right]. \end{aligned} \tag{74}$$

For an overlapping winding machine, the flux linkages in the *i*th slot are

$$\psi_{i1} = l_a \left(N_c/A_c\right) Z_{t0} b_{sa} \tag{75}$$

$$\psi_{i2} = l_a \left(N_c/A_c\right) Z_{b0} b_{sa} \tag{76}$$

where

$$\begin{aligned} Z_{t0} = & Q_{3ti}\left(R_{sm}^2 - {R_s}^2\right)/2 - \mu_0 J_{iam1}\left(R_{sm}^4 - {R_s}^4\right)/16 \\ & + \left(C_i + C_t\right)\left[2R_{sm}^2 \ln R_{sm}\right. \\ & \left. - 2{R_s}^2 \ln R_s + {R_s}^2 - R_{sm}^2\right]/4 \\ & - \mu_0 \left(J_{i1} + J_{i2}\right)\left(R_{sm}^3 - R_s^3\right)/\left(3b_{sa}\right) \end{aligned} \tag{77}$$

$$\begin{aligned} Z_{b0} = & Q_{3bi}\left(R_{sb}^2 - R_{sm}^2\right)/2 - \mu_0 J_{iam2}\left(R_{sb}^4 - R_{sm}^4\right)/16 \\ & - \mu_0 \left(J_{i1} + J_{i2}\right)\left(R_{sb}^3 - R_{sm}^3\right)/\left(3b_{sa}\right) \\ & + \left(C_i/4 + \mu_0 J_{iam2} R_{sb}^2/8\right) \\ & \cdot \left[2R_{sb}^2 \ln R_{sb} - 2R_{sn}^2 \ln R_{sn} + R_{sn}^2 - R_{sb}^2\right]. \end{aligned} \tag{78}$$

The back EMF also can be calculated after the flux linkage of every phase is obtained as follows:

$$E_{ph} = -d\psi_{ph}/dt \quad ph = A, B, C. \tag{79}$$

The total torque can be calculated from Maxwell stress tensor

$$T_c = \left(\pi l_a r^2/\mu_0\right) \sum_k \left(B_{rck} B_{\alpha ck} + B_{rsk} B_{\alpha sk}\right). \tag{80}$$

References

[1] Z. Q. Zhu and D. Howe, "Electrical machines and drives for electric, hybrid, and fuel cell vehicles," *Proc. IEEE*, vol. 95, no. 4, pp. 746–765, Apr. 2007.

[2] M. Andriollo, M. De Bortoli, G. Martinelli, A. Morini, and A. Tortella, "Design improvement of a single-phase brushless permanent magnet motor for small fan appliances," *IEEE Trans. Ind. Electron.*, vol. 57, no. 1, pp. 88–95, Jan. 2010.

[3] K. I. Laskaris and A. G. Kladas, "Internal permanent magnet motor design for electric vehicle drive," *IEEE Trans. Ind. Electron.*, vol. 57, no. 1, pp. 138–145, Jan. 2010.

[4] D. G. Dorrell, M.-F. Hsieh, M. Popescu, L. Evans, D. A. Staton, and V. Grout, "A review of the design issues and techniques for radial-flux brushless surface and internal rare-earth permanent-magnet motors," *IEEE Trans. Ind. Electron.*, vol. 58, no. 9, pp. 3741–3757, Sep. 2011.
[5] I.-C. Vese, F. Marignetti, and M. M. Radulescu, "Multiphysics approach to numerical modeling of a permanent-magnet tubular linear motor," *IEEE Trans. Ind. Electron.*, vol. 57, no. 1, pp. 320–326, Jan. 2010.
[6] L. Parsa and L. Hao, "Interior permanent magnet motors with reduced torque pulsation," *IEEE Trans. Ind. Electron.*, vol. 55, no. 2, pp. 602–609, Feb. 2008.
[7] J. Kolehmainen, "Optimal dovetail permanent magnet rotor solutions for various pole numbers," *IEEE Trans. Ind. Electron.*, vol. 57, no. 1, pp. 70–77, Jan. 2010.
[8] K. Yamazaki and H. Ishigami, "Rotor-shape optimization of interior-permanent-magnet motors to reduce harmonic iron losses," *IEEE Trans. Ind. Electron.*, vol. 57, no. 1, pp. 61–69, Jan. 2010.
[9] Z. Sun, J. Wang, D. Howe, and G. Jewell, "Analytical prediction of the short-circuit current in fault-tolerant permanent-magnet machines," *IEEE Trans. Ind. Electron.*, vol. 55, no. 12, pp. 4210–4217, Dec. 2008.
[10] C. K. Lim, I.-M. Chen, L. Yan, G. Yang, and K.-M. Lee, "Electromechanical modeling of a permanent-magnet spherical actuator based on magnetic-dipole-moment principle," *IEEE Trans. Ind. Electron.*, vol. 56, no. 5, pp. 1640–1648, May 2009.
[11] P.-D. Pfister and Y. Perriard, "Very-high-speed slotless permanent-magnet motors: analytical modeling, optimization, design, and torque measurement methods," *IEEE Trans. Ind. Electron.*, vol. 57, no. 1, pp. 296–303, Jan. 2010.
[12] Z. Q. Zhu, L. J. Wu, and Z. P. Xia, "An accurate subdomain model for magnetic field computation in slotted surface-mounted permanent-magnet machines," *IEEE Trans. Magn.*, vol. 46, no. 4, pp. 1100–1115, Apr. 2010.
[13] P.-D. Pfister, X. Yin, and Y. Fang, "Slotted permanent-magnet machines: General analytical model of magnetic fields, torque, eddy currents, and permanent-magnet power losses including the diffusion effect," *IEEE Trans. Magn.*, vol. 52, no. 5, pp. 1–13, May 2016.
[14] Z. Q. Zhu, D. Howe, E. Bolte, and B. Ackermann, "Instantaneous magnetic field distribution in brushless permanent magnet dc motors, Part I: Open-circuit field," *IEEE Trans. Magn.*, vol. 29, no. 1, pp. 124–135, Jan. 1993.
[15] Z. Q. Zhu and D. Howe, "Instantaneous magnetic field distribution in brushless permanent magnet dc motors, Part II: Armature-reaction field," *IEEE Trans. Magn.*, vol. 29, no. 1, pp. 136–142, Jan. 1993.
[16] Z. Q. Zhu and D. Howe, "Instantaneous magnetic field distribution in brushless permanent magnet dc motors, Part III: Effect of stator slotting," *IEEE Trans. Magn.*, vol. 29, no. 1, pp. 143–151, Jan. 1993.
[17] Z. Q. Zhu and D. Howe, "Instantaneous magnetic field distribution in permanent magnet brushless dc motors, Part IV: Magnetic field on load," *IEEE Trans. Magn.*, vol. 29, no. 1, pp. 152–158, Jan. 1993.
[18] D. Zarko, D. Ban, and T. A. Lipo, "Analytical calculation of magnetic field distribution in the slotted air gap of a surface permanent-magnet motor using complex relative air-gap permeance," *IEEE Trans. Magn.*, vol. 42, no. 7, pp. 1828–1837, Jul. 2006.
[19] D. Zarko, D. Ban, and T. A. Lipo, "Analytical solution for cogging torque in surface permanent-magnet motors using conformal mapping," *IEEE Trans. Magn.*, vol. 44, no. 1, pp. 52–65, Jan. 2008.
[20] L. J. Wu, Z. Q. Zhu, D. Staton, M. Popescu, and D. Hawkins, "An improved subdomain model for predicting magnetic field of surface-mounted permanent magnet machines accounting for tooth-tips," *IEEE Trans. Magn.*, vol. 47, no. 6, pp. 1693–1704, Jun. 2011.
[21] L. J. Wu, Z. Q. Zhu, D. Staton, M. Popescu, and D. Hawkins, "Subdomain model for predicting armature reaction field of surface-mounted permanent-magnet machines accounting for tooth-tips," *IEEE Trans. Magn.*, vol. 47, no. 4, pp. 812–822, Apr. 2011.
[22] L. J. Wu, Z. Q. Zhu, D. Staton, M. Popescu, and D. Hawkins, "Analytical prediction of electromagnetic performance of surface-mounted PM machines based on subdomain model accounting for tooth-tips," *IET Electr. Power Appl.*, vol. 5, no. 7, pp. 597–609, Aug. 2011.
[23] E. Devillers, J. Le Besnerais, T. Lubin, M. Hecquet, and J. Lecointe, "A review of subdomain modeling techniques in electrical machines: Performances and applications," in *Proc. 22nd Int. Conf. Elect. Mach.*, Sep. 2016, pp. 86–92.
[24] J. Hur, S.-B. Yoon, D.-Y. Hwang, and D.-S. Hyun, "Analysis of PMLSM using three dimensional equivalent magnetic circuit network method," *IEEE Trans. Magn.*, vol. 33, no. 5, pp. 4143–4145, Sep. 1997.
[25] S.-H. Lee, S.-O. Kwon, J.-J. Lee, and J.-P. Hong, "Characteristic analysis of claw-pole machine using improved equivalent magnetic circuit," *IEEE Trans. Magn.*, vol. 45, no. 10, pp. 4570–4573, Oct. 2009.
[26] K.-D. Lee, J. Lee, and H.-W. Lee, "Inductance calculation of flux concentrating permanent magnet motor through nonlinear magnetic equivalent circuit," *IEEE Trans. Magn.*, vol. 51, no. 11, pp. 1–4, Nov. 2015.
[27] F. R. Alam and K. Abbaszadeh, "Magnetic field analysis in eccentric surface-mounted permanent-magnet motors using an improved conformal mapping method," *IEEE Trans. Energy Convers.*, vol. 31, no. 1, pp. 333–344, Mar. 2016.
[28] F. Rezaee-Alam, B. Rezaeealam, and J. Faiz, "Unbalanced magnetic force analysis in eccentric surface permanent-magnet motors using an improved conformal mapping method," *IEEE Trans. Energy Convers.*, vol. 32, no. 1, pp. 146–154, Mar. 2017.
[29] A. Hanic, D. Zarko, and Z. Hanic, "A novel method for no-load magnetic field analysis of saturated surface permanent-magnet machines using conformal mapping and magnetic equivalent circuits," *IEEE Trans. Energy Convers.*, vol. 31, no. 2, pp. 740–749, Jun. 2016.
[30] A. Hanic, D. Zarko, D. Kuhinek, and Z. Hanic, "On-load analysis of saturated surface permanent magnet machines using conformal mapping and magnetic equivalent circuits," *IEEE Trans. Energy Convers.*, vol. 33, no. 3, pp. 915–924, Sep. 2018.
[31] L. J. Wu, Z. Li, X. Huang, Y. Zhong, Y. Fang, and Z. Q. Zhu, "A hybrid field model for open-circuit field prediction in surface-mounted PM machines considering saturation," *IEEE Trans. Magn.*, vol. 54, no. 6, pp. 1–12, Jun. 2018.
[32] A. Hemeida and P. Sergeant, "Analytical modeling of surface PMSM using a combined solution of Maxwell's equations and magnetic equivalent circuit," *IEEE Trans. Magn.*, vol. 50, no. 12, Dec. 2014, Art. no. 7027913.
[33] E. Ilhan, B. L. J. Gysen, J. J. H. Paulides, and E. A. Lomonova, "Analytical hybrid model for flux switching permanent magnet machines," *IEEE Trans. Magn.*, vol. 46, no. 6, pp. 1762–1765, Jun. 2010.
[34] S. Ouagued, A. A. Diriye, Y. Amara, and G. Barakat, "A general framework based on a hybrid analytical model for the analysis and design of permanent magnet machines," *IEEE Trans. Magn.*, vol. 51, no. 11, Nov. 2015, Art. no. 8110204.
[35] Y. Laoubi, M. Dhifli, G. Verez, Y. Amara, and G. Barakat, "Open circuit performance analysis of a permanent magnet linear machine using a new hybrid analytical model," *IEEE Trans. Magn.*, vol. 51, no. 3, Mar. 2015, Art. no. 8102304.
[36] S. Ouagued, Y. Amara, and G. Barakat, "Cogging force analysis of linear permanent magnet machines using a hybrid analytical model," *IEEE Trans. Magn.*, vol. 52, no. 7, Jul. 2016, Art. No. 8202704.
[37] L. Wu, H. Yin, D. Wang, and Y. Fang, "A nonlinear subdomain and magnetic circuit hybrid model for open-circuit field prediction in surface-mounted PM machines," *IEEE Trans. Energy Convers.*, vol. 34, no. 3, pp. 1485–1495, Sep. 2019.

Lijian Wu (M'11–SM'14) received the B.Eng. and M.Sc. degrees from the Hefei University of Technology, Hefei, China, in 2001 and 2004, respectively, and the Ph.D. degree from the University of Sheffield, Sheffield, U.K., in 2011, all in electrical engineering.

From 2004 to 2007, he was an Engineer with Delta Electronics (Shanghai) Company, Ltd. From 2012 to 2013, he was a Design Engineer with Sheffield Siemens Wind Power Research Center focusing on the wind power generators. From 2013 to 2016, he was an Advanced Engineer with Siemens Wind Power A/S, Brande, Denmark. Since 2016, he has been with Zhejiang University, Hangzhou, China, where he is currently a Professor of Electrical Machines and Control Systems. His current research interest include the design and control of permanent magnet machines.

Hao Yin received the B.Eng. degree in electrical engineering in 2017 from Zhejiang University, Hangzhou, China, where he is currently working toward the M.Sc. degree in electrical engineering.

His current major research interest focuses on the design and analysis of permanent magnet machines.

Dong Wang was born in Wuhan, China, in 1978. He received the B.Eng. and Ph.D. degrees in electrical engineering from the Naval University of Engineering, Wuhan, China, in 2000 and 2007, respectively.

He is currently a Professor of Electrical Machines and Control Systems and a Supervisor for doctoral candidates with the Naval University of Engineering. His current research interests include electric propulsion and the integrated power generation systems.

Youtong Fang (M'11–SM'15) received the B.S. and Ph.D. degrees in electrical engineering from the Hebei University of Technology, Hebei, China, in 1984 and 2001 respectively.

He is currently a Professor of Electrical Machines and Control Systems with the College of Electrical Engineering, Zhejiang University, Hangzhou, China. His research interests include application, control, and design of electrical machines.